Quadrupole-octupole coupling and the onset of octupole deformation in actinides

K. Nomura [1,*] R. Rodríguez-Guzmán [2] L. M. Robledo [3,4] and J. E. García-Ramos [5,6]

[1]*Department of Physics, Faculty of Science, University of Zagreb, Zagreb HR-10000, Croatia*
[2]*Physics Department, Kuwait University, 13060 Kuwait, Kuwait*
[3]*Departamento de Física Teórica and CIAFF, Universidad Autónoma de Madrid, E-28049 Madrid, Spain*
[4]*Center for Computational Simulation, Universidad Politécnica de Madrid, Campus de Montegancedo, Bohadilla del Monte, E-28660 Madrid, Spain*
[5]*Departamento de Ciencias Integradas y Centro de Estudios Avanzados en Física, Matemática y Computación, Universidad de Huelva, E-21071 Huelva, Spain*
[6]*Instituto Carlos I de Física Teórica y Computacional, Universidad de Granada, Fuentenueva s/n, 18071 Granada, Spain*

(Received 3 February 2021; accepted 29 March 2021; published 12 April 2021)

The evolution of quadrupole and octupole collectivity and their coupling is investigated in a series of even-even isotopes of the actinides Ra, Th, U, Pu, Cm, and Cf with neutron number in the interval $130 \leqslant N \leqslant 150$. The Hartree-Fock-Bogoliubov approximation, based on the parametrization D1M of the Gogny energy density functional, is employed to generate potential energy surfaces depending upon the axially symmetric quadrupole and octupole shape degrees of freedom. The mean-field energy surface is then mapped onto the expectation value of the *sdf* interacting-boson-model Hamiltonian in the boson condensate state as to determine the strength parameters of the boson Hamiltonian. Spectroscopic properties related to the octupole degree of freedom are produced by diagonalizing the mapped Hamiltonian. Calculated low-energy negative-parity spectra, $B(E3; 3_1^- \rightarrow 0_1^+)$ reduced transition rates, and effective octupole deformation suggest that the transition from nearly spherical to stable octupole-deformed, and to octupole vibrational states occurs systematically in the actinide region.

DOI: 10.1103/PhysRevC.103.044311

I. INTRODUCTION

Over the decades, octupole deformation in nuclei and the related spectroscopy of negative-parity collective states has been an active research field in low-energy nuclear physics [1,2]. It is well known that the ground state of most medium-mass and heavy nuclei is reflection symmetric and therefore the dominant intrinsic deformation is of quadrupole character. However, there are a handful of nuclear systems where reflection symmetry is broken, giving rise to an octupole-deformed ground state. The octupole shape is expected to be present in those mass regions corresponding to protons Z and neutron numbers N close to 34, 56, 88, and 134 [1,2]. Observables characteristic of the ground-state static octupole deformation are low-lying negative-parity bands, which form well-deformed quadrupole deformed nuclei and approximate alternating-parity doublets with the ground-state positive-parity band, and enhanced electric dipole and octupole transition rates. Fingerprints of stable octupole shapes have been found experimentally in light actinides (^{220}Rn, ^{224}Ra, ^{222,228}Ra [3,4], and ^{228}Th [5]) and lanthanides (^{144,146}Ba [6,7]). Within this context, numerous theoretical investigations have been made to predict, and support evidence of, octupole deformation by means of various theoretical models: macroscopic-microscopic models [8–10], self-consistent mean-field (SCMF) methods based on the nuclear density functional theory [11–38], the interacting boson model (IBM) [39–45], geometrical collective models [46–48], and cluster models [49,50].

Octupole collective excitations in the light actinide nuclei with $Z \approx 88$ and $N \approx 134$ have been extensively studied both experimentally and theoretically. However, spectroscopic data for those actinide nuclei heavier than Th, such as Pu, Cm, and Cf isotopes, are scarce, especially in the neutron-deficient side of the nuclear chart with $N \approx 134$. This is because these isotopes are close to the proton drip line and have not been accessible so far by experiments. It is, nevertheless, worth to explore theoretically whether the robustness of the neutron octupole magic number $N = 134$ in actinides holds when one departs from $Z \approx 88$ towards the proton drip line.

In the present work, we employ the energy density functional (EDF)-to-IBM mapping procedure [51] for a theoretical calculation of the properties of octupole collective excitations. This procedure involves two main steps: First, for each nucleus a potential energy surface (PES) depending upon the axially symmetric quadrupole β_2 and octupole β_3 shape degrees of freedom is computed within the constrained SCMF method with a choice of a universal energy density functional and pairing force. In a second step, the PES is mapped onto the expectation value of the bosonic Hamiltonian in the condensate state of the monopole s, quadrupole d, and octupole f bosons in order to fix some of the model's parameters [39,52]. Subsequent diagonalization of the

*knomura@phy.hr

 ©2021 American Physical Society

resulting boson Hamiltonian yields excitation energy spectra and transition strengths. The mapping procedure has been initially implemented [42,43] in the study of spectroscopic properties of reflection-asymmetric Ba, Sm, Ra, and Th nuclei using the relativistic density-dependent point-coupling (DD-PC1) EDF [53] to generate the microscopic PES. More recently, updated calculations have been performed [45] in the $^{218–238}$Ra and $^{220–240}$Th isotopic chains within the mapped IBM framework based on the Gogny D1M EDF [54]. In those studies, consistent with the empirical trend, we have identified a most pronounced octupolarity around the neutron number $N = 134$ in the systematic of calculated physical observables.

In view of the renewed interest in a global search for the static octupole deformation beyond Ra and Th isotopes, here we extend the analysis of Ref. [45] to heavier actinide nuclei $^{222–242}$U, $^{224–244}$Pu, $^{226–246}$Cm, and $^{228–248}$Cf, and verify whether the octupole-related shape phase transition generally occurs in the actinide region, that is, the onset of stable octupole deformation at $N \approx 134$ and octupole softness starting from $N \approx 138$. With the present study we also aim to assess the performance of the EDF-based IBM approach in the global description of octupole collective states in the actinide region. The results further include quantitative predictions on spectroscopy in proton-rich actinides that have not been explored so far by experiment. This has not been possible in the previous IBM calculations, since they are mostly fit to known experimental data. Hence, the present work points not only to an alternative EDF-based approach to the detailed spectroscopy of a large number of actinide nuclei, but it is a first implementation of the IBM framework in the octupole-related spectroscopic studies on proton-rich heavy actinides, that is based on the microscopic EDF.

It should be noted that interplay between quadrupole and octupole degrees of freedom in the low-lying negative-parity collective states of U, Pu, Cm, and Cf nuclei has also been studied within the framework of the generator coordinate method (GCM) [55–57] using the Gogny D1M EDF [38]. The GCM calculation is, however, quite time consuming especially for heavy systems or when the number of collective coordinates increases. Computational complexity also prevents access to high spin states like, for instance, the members of alternating-parity rotational bands. In Refs. [33,34], a large number of heavy and superheavy nuclei up to No isotopes with mass $A \approx 300$ have been analyzed by solving quadrupole-octupole collective Hamiltonians, with parameters specified by the relativistic EDF calculations. Detailed spectroscopy of stable U and Pu nuclei was explored within a purely phenomenological *spdf*-IBM framework in Refs. [41,58].

The paper is organized as follows. The mapping procedure used to obtain the IBM Hamiltonian is illustrated in Sec. II. The results of our analysis are discussed in Sec. III, including the Gogny-D1M quadrupole-octupole SCMF-PESs, i.e., the microscopic building blocks of the calculations, mapped IBM-PESs, low-energy excitation spectra, transition properties, and the effective β_2 and β_3 deformation parameters. Finally, Sec. IV is devoted to the concluding remarks and work perspectives.

II. THEORETICAL METHOD

To obtain the quadrupole-octupole SCMF-PESs, the Hartree-Fock-Bogoliubov (HFB) equation has been solved with constraints on the axially symmetric quadrupole $\hat{Q}_{20}$ and octupole $\hat{Q}_{30}$ operators [27,38]. The mean values $\langle\Phi_{\rm HFB}|\hat{Q}_{20}|\Phi_{\rm HFB}\rangle = Q_{20}$ and $\langle\Phi_{\rm HFB}|\hat{Q}_{30}|\Phi_{\rm HFB}\rangle = Q_{30}$ define the quadrupole and octupole deformation parameters β_λ ($\lambda = 2, 3$), i.e., $\beta_\lambda = \sqrt{4\pi(2\lambda+1)}Q_{\lambda 0}/(3R_0^\lambda A)$, with $R_0 = 1.2A^{1/3}$ fm. The constrained calculations provide a set of HFB states $|\Phi_{\rm HFB}(\beta_2, \beta_3)\rangle$ labeled by their static deformation parameters β_2 and β_3. The HFB energies $E_{\rm HFB}(\beta_2, \beta_3)$ associated with those HFB states define the so-called SCMF-PESs used in this work. As the HFB energies satisfy the property $E_{\rm HFB}(\beta_2, \beta_3) = E_{\rm HFB}(\beta_2, -\beta_3)$ only positive β_3 values are considered when plotting the SCMF-PESs.

Excitation energies and transition probabilities of the quadrupole and octupole collective states are computed by diagonalizing the IBM Hamiltonian that is determined with microscopic input from the Gogny-HFB SCMF calculation (see below). For computing negative-parity states, we consider the $J = 0^+$ (s), $J = 2^+$ (d), and $J = 3^-$ (f) bosons as building blocks of the IBM. The total number of bosons $n = n_s + n_d + n_f$ is conserved for a given nucleus, and is equal to half the number of valence nucleons. The doubly-magic nucleus ^{208}Pb is taken here as the inert core, and thus $n = (A - 208)/2$ for a nucleus with mass A. We adopt the *sdf*-IBM Hamiltonian [45]:

$$\hat{H}_{\rm IBM} = \epsilon_d \hat{n}_d + \epsilon_f \hat{n}_f + \kappa_2 \hat{Q}_2 \cdot \hat{Q}_2 + \rho \hat{L} \cdot \hat{L} + \kappa_3 \hat{Q}_3 \cdot \hat{Q}_3. \tag{1}$$

The first (second) term represents the number operator for the d (f) bosons with ϵ_d (ϵ_f) being the single d (f) boson energy relative to the s boson one. The third, fourth, and fifth terms represent the quadrupole-quadrupole interaction, the rotational term, and the octupole-octupole interaction, respectively. The quadrupole $\hat{Q}_2$, the angular momentum $\hat{L}$, and the octupole $\hat{Q}_3$ operators are expressed as

$$\hat{Q}_2 = s^\dagger \tilde{d} + d^\dagger \tilde{s} + \chi_d [d^\dagger \times \tilde{d}]^{(2)} + \chi_f [f^\dagger \times \tilde{f}]^{(2)}, \tag{2}$$

$$\hat{L} = \sqrt{10}[d^\dagger \times \tilde{d}]^{(1)} + \sqrt{28}[f^\dagger \times \tilde{f}]^{(1)}, \tag{3}$$

$$\hat{Q}_3 = s^\dagger \tilde{f} + f^\dagger \tilde{s} + \chi_3 [d^\dagger \times \tilde{f} + f^\dagger \times \tilde{d}]^{(3)}. \tag{4}$$

Note that the term proportional to $(d^\dagger \tilde{d})^{(1)} \cdot (f^\dagger \tilde{f})^{(1)}$ in the $\hat{L} \cdot \hat{L}$ term has been neglected [45]. The parameters ϵ_d, ϵ_f, κ_2, ρ, χ_d, χ_f, κ_3, and χ_3 of the *sdf*-IBM Hamiltonian are determined, for each nucleus, in such a way [44,45] that the expectation value of the *sdf*-IBM Hamiltonian in the boson condensate state, $E_{\rm IBM}(\beta_2, \beta_3) = \langle\phi(\beta_2, \beta_3)|\hat{H}_{\rm IBM}|\phi(\beta_2, \beta_3)\rangle$, reproduces the Gogny-HFB SCMF-PES $E_{\rm HFB}(\beta_2, \beta_3)$ in the neighborhood of the global minimum. The boson condensate wave function is given by [59]

$$|\phi(\beta_2, \beta_3)\rangle = (n!)^{-1/2}(s^\dagger + \bar{\beta}_2 d_0^\dagger + \bar{\beta}_3 f_0^\dagger)^n |0\rangle, \tag{5}$$

where $|0\rangle$ denotes the inert core, i.e., ^{208}Pb. The amplitudes $\bar{\beta}_2$ and $\bar{\beta}_3$ entering the definition of the boson condensate wave function are proportional to the deformation parameters β_2 and β_3 of the fermionic space, $\bar{\beta}_2 = C_2\beta_2$ and $\bar{\beta}_3 = C_3\beta_3$ [43,44,59], with dimensionless proportionality constants C_2

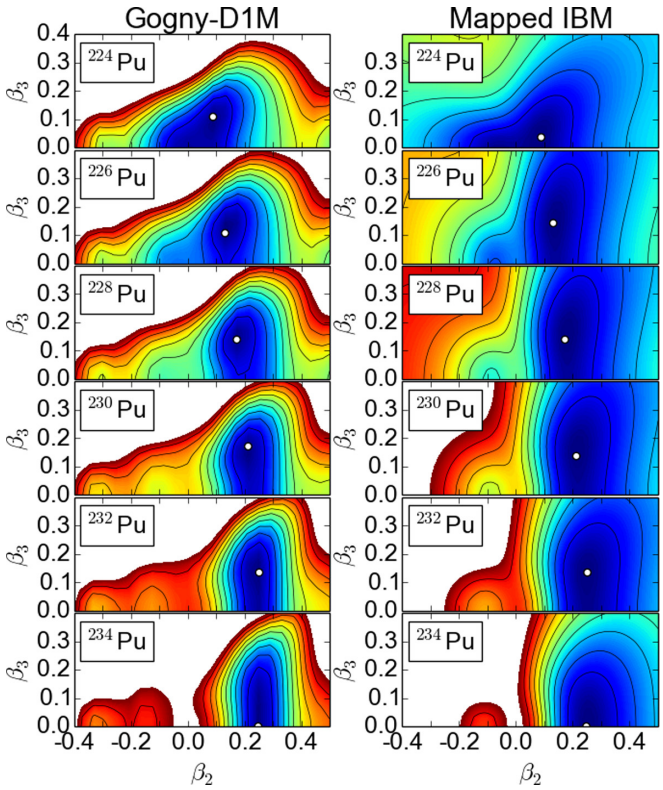

FIG. 1. SCMF-PESs computed with the Gogny-D1M EDF for the nuclei $^{224-234}$Pu (left), and the corresponding mapped *sdf*-IBM PESs (right). The color code indicates the total HFB and IBM energies in MeV units, plotted up to 10 MeV with respect to the global minimum. The energy difference between neighboring contours is 1 MeV. For each nucleus, the global minimum is indicated by an open circle.

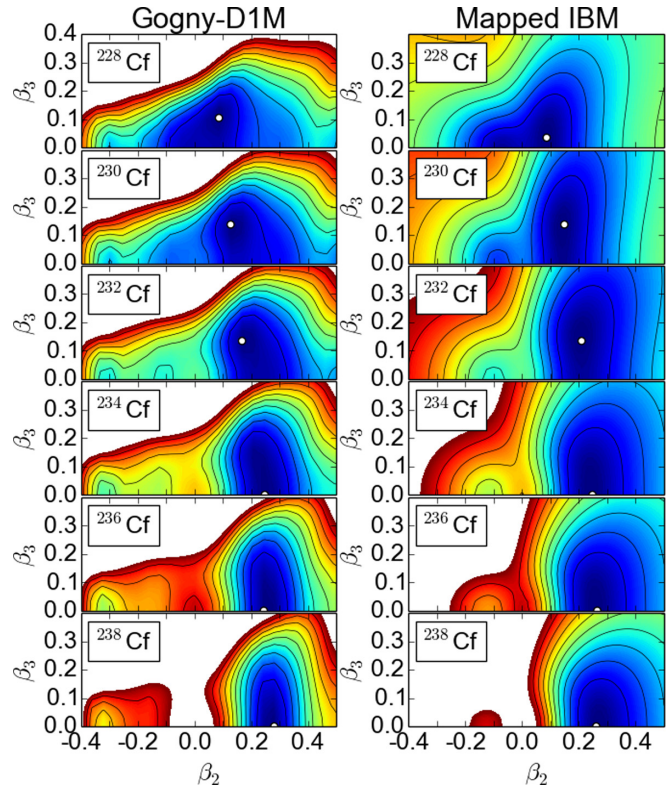

FIG. 2. Same as for Fig. 1, but for $^{248-238}$Cf.

and C_3. Their values are also determined by the mapping procedure so that the location of the global minimum in the SCMF-PES, denoted by $\beta_{2,\min}$ and $\beta_{3,\min}$, is reproduced. A more detailed description of the whole procedure can be found in Ref. [45]. As for the analytical expression of the IBM-PES $E_{\rm IBM}(\beta_2, \beta_3)$, we refer the reader to Ref. [44].

For the numerical diagonalization of the Hamiltonian $\hat{H}_{\rm IBM}$ (1), the computer code ARBMODEL [60] has been used.

III. RESULTS AND DISCUSSIONS

A. Gogny-D1M SCMF-PESs

As representative cases, the Gogny-D1M SCMF-PESs for $^{224-234}$Pu and $^{228-238}$Cf are depicted in the left-hand columns of Figs. 1 and 2, respectively. In most of the Pu isotopes, a nonzero β_3 minimum $\beta_{3,\min}$ is found in the interval $0.1 \leqslant \beta_3 \leqslant 0.2$. The most pronounced octupole minimum is obtained at $N = 134$ (^{228}Pu) around $\beta_{3,\min} \approx 0.17$. For Cf nuclei in Fig. 2, only three isotopes are octupole deformed with $\beta_{3,\min} < 0.15$. Note that for those isotopes with $N > 140$, the potential energy becomes softer in β_3 and no octupole deformation is found.

The systematic of the SCMF-PESs for U and Cm isotopes is similar to the one for Pu and Cf isotopes, and the PESs for Ra and Th can be found in Ref. [45]. It is also worth mentioning that the Gogny-D1M SCMF-PESs used in this paper are very similar to those obtained in Ref. [26] using the Gogny-D1S [61] and D1N [62], and the Barcelona-Catania-Paris (BCP) [23] EDFs. Recent comparisons of several nonrelativistic Skyrme and relativistic EDFs in a survey of octupole correlations can be found in Refs. [37] and [31], respectively. In those references, it is noticed that for most of the adopted EDFs pronounced octupole mean-field minima occur around $N = 134$.

B. Mapped IBM-PESs

The corresponding IBM-PESs are shown on the right-hand sides of Figs. 1 and 2. One can clearly observe the similarities between the SCMF and IBM PESs: the topography of the IBM-PES changes with the neutron number in a similar way as the SCMF-PES, from nearly spherical configurations ($N \approx 130$) to pronounced octupole deformation ($N \approx 134$) continuing with β_3 soft ($N \approx 138$). The IBM-PESs are generally softer than the SCMF-PESs. This is related to the more restricted configuration space of the IBM as compared to the one of the SCMF model.

In Fig. 3 we show, as a function of neutron number, the values of several quantities characterizing the self-consistent minima found in the IBM (left panels) and SCMF-PES (right panels). In Figs. 3(a) and 3(b) the values of the quadrupole and octupole deformation parameters of the absolute minimum $\beta_{2,\min}$ and $\beta_{3,\min}$ are plotted. In Fig. 3(c) the quadrupole deformation energy $\Delta E_{\rm def}$, defined as the energy

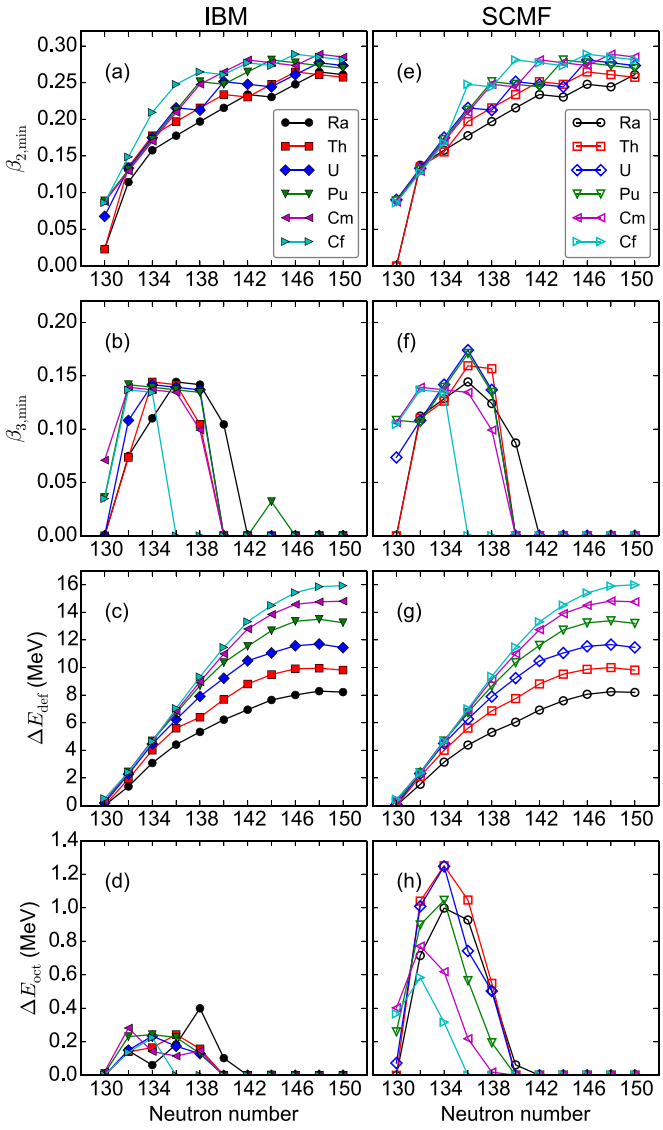

FIG. 3. The (a) $\beta_{2,\min}$ and (b) $\beta_{3,\min}$ values, corresponding to the ground-state minimum, are plotted as a function of neutron number. (c) The deformation energy $\Delta E_{\rm def}$, defined as the energy difference between the global minimum and the spherical configuration, is plotted as a function of neutron number. (d) The octupole deformation energy $\Delta E_{\rm oct}$, defined as the energy difference between the global minimum and the quadrupole deformed minimum along the $\beta_3 = 0$ axis, for the mapped IBM-PESs is plotted. (e)–(h) The corresponding quantities for the SCMF-PESs are also plotted on the right-hand side. The results for the Ra and Th nuclei are taken from Ref. [45]. See the main text for definitions of the above quantities.

difference between the energy at the global minimum and at the spherical point,

$$\Delta E_{\rm def} = E(\beta_{2,\min}, \beta_{3,\min}) - E(0, 0), \tag{6}$$

is shown, where $E(\beta_2, \beta_3)$ refers either to the SCMF-PES or the IBM-PES. Finally, the octupole deformation energies $\Delta E_{\rm oct}$, defined as the energy difference between the energy at the global minimum and the local minimum on the $\beta_3 = 0$ axis, i.e.,

$$\Delta E_{\rm oct} = E(\beta_{2,\min}, \beta_{3,\min}) - E(\beta'_{2,\min}, 0), \tag{7}$$

are shown in Fig. 3(d). In the above expression $\beta'_{2,\min}$ stands for the β_2 deformation parameter corresponding to the local minimum on the $\beta_3 = 0$ axis. The corresponding quantities calculated with the SCMF-PESs $E_{\rm HFB}(\beta_2, \beta_3)$ are included in Figs. 3(e)–3(h). The systematic as a function of neutron number of most of these quantities is basically the same when looking at the SCMF- and IBM-PESs.

Only one exception can be seen in the quantity $\Delta E_{\rm oct}$ shown in Fig. 3(d): the IBM values are a factor of between 2 to 5 lower than the SCMF ones. This discrepancy reflects the fact that the IBM-PESs are much softer in β_3 direction than the SCMF-PESs: the latter displays a much steeper potential in β_3 than the former (see also Figs. 1 and 2). It is partly attributed to the fact that the analytical form of the IBM-PES [44] is so restricted, comprising only a limited number and species of bosons, that it is not able to reproduce in full detail the topology of the SCMF-PES, which is much steeper in the β_3 direction, but only the overall topology of the SCMF-PES typically up to a few MeV from the minimum. However, the SCMF solutions within this energy range are most relevant to low-lying states. In addition, the fact that the IBM-PESs are considerably β_3 soft as compared to the SCMF ones presents a general feature of the IBM framework, but is considered to be of minor relevance to reproducing spectroscopic properties of a low-energy yrast state and thus does not alter the main conclusions.

C. Derived IBM parameters

In Fig. 4 we display the IBM parameters obtained for the considered U, Pu, Cm, and Cf nuclei as functions of the neutron number N. Most of the derived parameters appear to stay nearly constant with N, and their values also do not significantly differ between different isotopic chains. This is conceptually very satisfying as it indicates the consistency of the approach and its predictive power. An exception is perhaps the f-boson energy ϵ_f depicted in Fig. 4(b), which exhibits an abrupt structural change between neighboring isotopes. The rapid decrease of the quantity $-\epsilon_f$ from $N = 130$ to 136 indicates the development of the octupole collectivity.

D. Evolution of low-energy excitation spectra

The excitation spectra for the low-lying even-spin positive-parity and odd-spin negative-parity yrast states of $^{222-242}$U, $^{224-244}$Pu, $^{226-246}$Cm, and $^{228-248}$Cf are depicted in Figs. 5 and 6 as functions of N, respectively. In Fig. 5, the calculated positive-parity levels in each isotopic chain [Figs. 5(a_1)–5(d_1)] are seen to decrease from $N = 130$ to 134, as the quadrupole collectivity develops. A typical rotational band structure starts to appear from $N \approx 132$, and there is no significant change in positive-parity states from $N = 134$ on. Agreement between the theoretical and experimental [Figs. 5(a_2)–5(d_2)] positive-parity levels is remarkable. It should be noted that the predicted level structure of the transitional nuclei with $N = 130$ and 132 looks rather irregular:

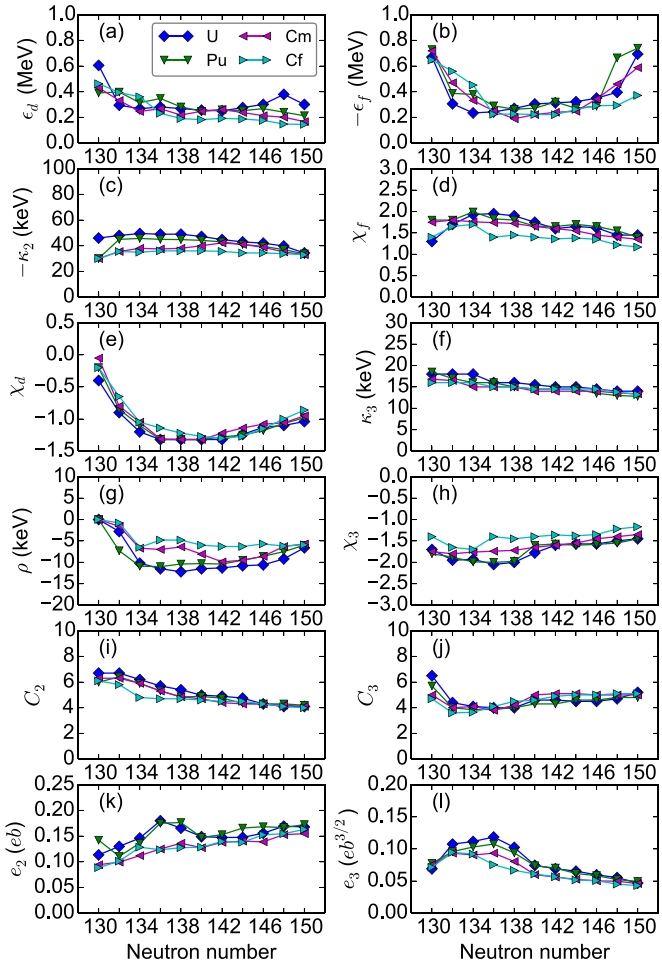

FIG. 4. The strength parameters (a) ϵ_d, (b) ϵ_f, (c) κ_2, (d) χ_f, (e) χ_d, (f) κ_3, (g) ρ, and (h) χ_3 of the *sdf*-IBM Hamiltonian, Eq. (1), are plotted as a function of neutron number for the four isotopic chains considered. The coefficients (i) C_2 and (j) C_3 connecting the IBM and microscopic quadrupole and octupole deformation parameters are plotted. Finally, the boson effective charges for the (k) quadrupole e_2 and (l) octupole e_3 transitions are plotted as a function of the neutron number. The parameters for Ra and Th isotopes can be found in Ref. [45].

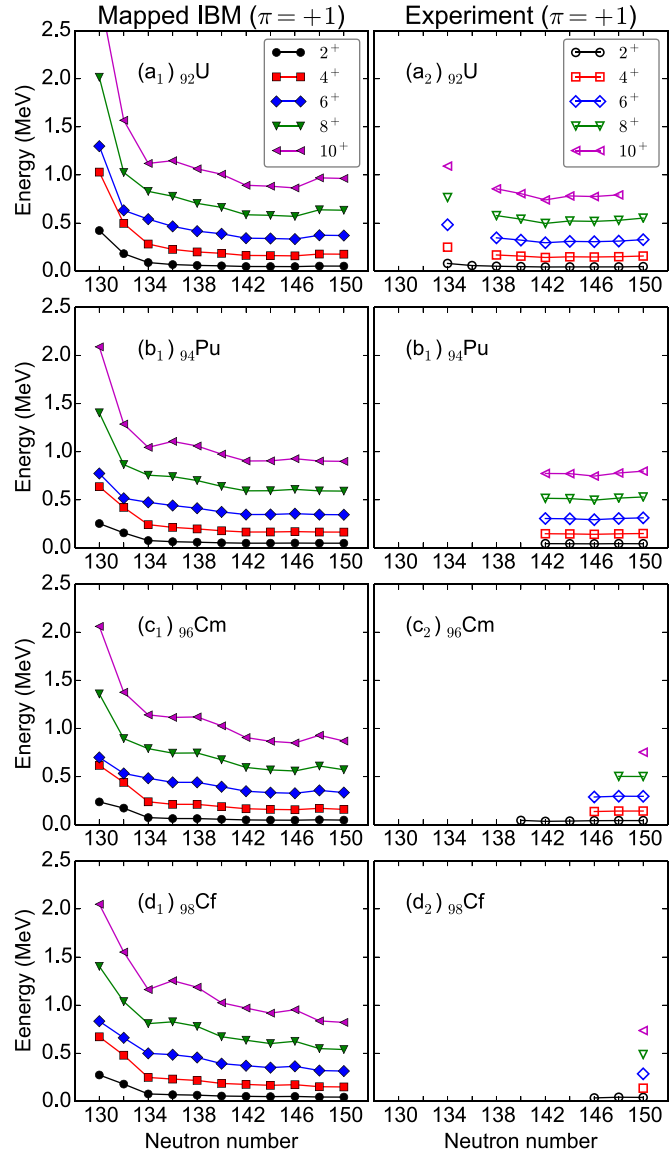

FIG. 5. Low-energy excitation spectra of positive-parity even-spin yrast states of $^{222–242}$U, $^{224–244}$Pu, $^{226–246}$Cm, and $^{228–248}$Cf computed by the diagonalization of the mapped *sdf*-IBM Hamiltonian, Eq. (1). Experimental data are taken from Ref. [63]. Results for Ra and Th isotopes can be found in Ref. [45].

energy levels of the 4_1^+ and 6_1^+ are close to each other, at variance with the well-known vibrational or rotational band patterns. As we show in Sec. III E, such an irregularity in the calculated levels seems to occur due to strong mixing between positive- and negative-parity boson configurations in the low-spin states of these nuclei.

The systematic behavior of the calculated negative-parity states is depicted in Figs. 6(a_1)–6(d_1). The comparison of our results with the available experimental data [Figs. 6(a_2)–6(d_2)] is reasonable. For each considered isotopic chain, the predicted negative-parity states exhibit an approximate parabolic behavior centered around $N = 134$ which corresponds with the nuclei where the octupole minimum is most pronounced in the SCMF-PESs. From $N = 134$ on, the negative-parity level energies keep increasing up to $N = 142$, where another paraboliclike behavior sets in the U, Pu, and Cf isotopes. The absence of permanent octupole deformation in those isotopes hints to an increasing dominant role of dynamic octupole correlations.

E. f-boson contribution to low-lying states

Next, we discuss the contribution of the f boson to the wave functions of the low-lying positive- and negative-parity states. Figure 7 displays the expectation values of the f-boson number operator $\langle \hat{n}_f \rangle$ computed in the IBM wave functions of the states 0_1^+, 2_1^+, 0_2^+, 2_2^+, 1_1^-, and 3_1^-. From Figs. 7(a) and 7(b), we learn that the expectation value $\langle \hat{n}_f \rangle$ is rather large in the transitional region $132 \leqslant N \leqslant 138$ indicating that the mixing between the *s-d* and f boson spaces is significant

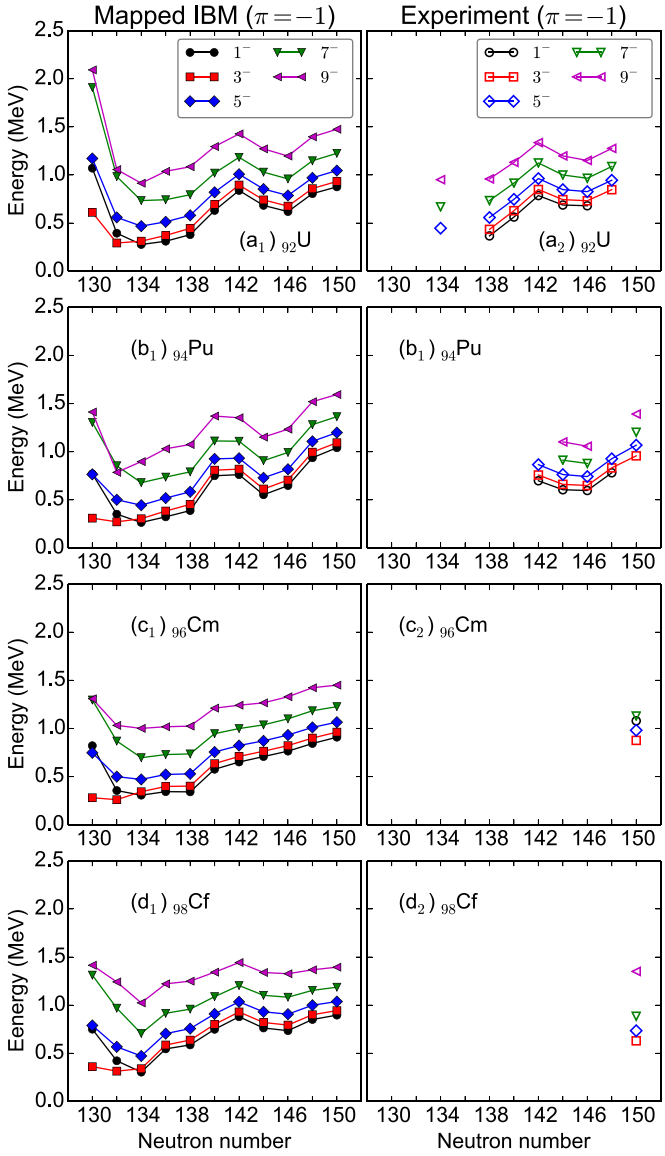

FIG. 6. Same as the caption of Fig. 5, but for the odd-spin negative-parity yrast states.

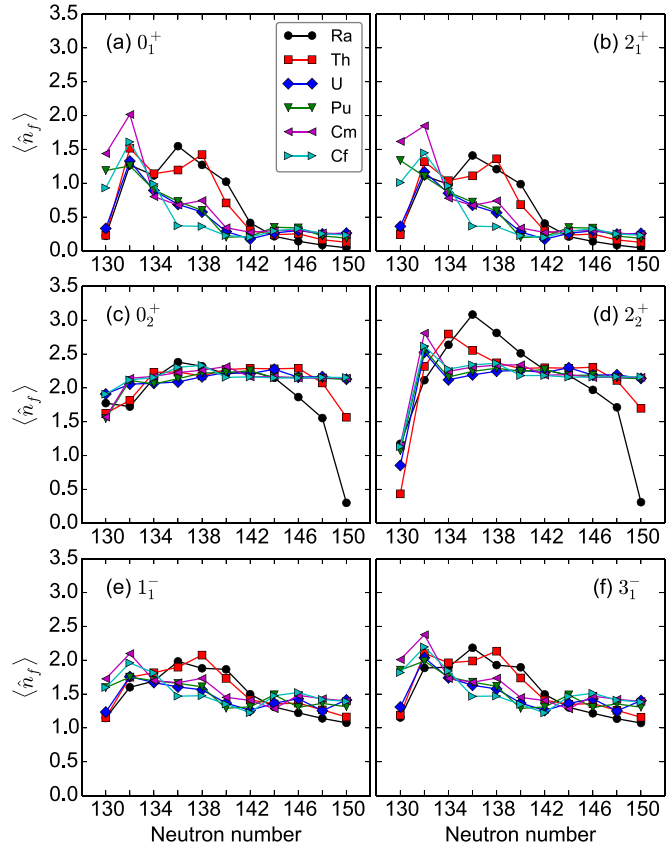

FIG. 7. Expectation values of the f-boson number operator $\langle \hat{n}_f \rangle$ in the IBM wave functions of the states 0_1^+, 2_1^+, 0_2^+, 2_2^+, 1_1^-, and 3_1^- of the Ra, Th, U, Pu, Cm, and Cf nuclei, plotted as functions of the neutron number. The values for the Ra and Th isotopes are taken from Ref. [45].

in the ground-state band. There is a marked difference in the results between the Ra and Th isotopes and the U, Pu, Cm, and Cf isotopes with the neutron numbers $136 \leqslant N \leqslant 140$: the f-boson contributions to the ground-state bands of the U, Pu, Cm, and Cf isotopes are by a factor of 2 to 5 smaller than for the Ra and Th nuclei. Thus it follows that, in the present framework, the quadrupole-octupole correlations become weaker as the proton number increases. For N larger than 140, both the 0_1^+ and 2_1^+ states are made of the s and d bosons alone, as the expectation values $\langle \hat{n}_f \rangle \approx 0$.

By looking at Figs. 7(c) and 7(d), we conclude that the structure of the wave functions of the 0_2^+ and 2_2^+ states corresponds to a double-octupole phonon structure as the expectation value $\langle \hat{n}_f \rangle \approx 2$. Empirical studies have interpreted that low-energy $K = 0^+$ excited bands in the actinide region are partly accounted for by the coupling between double octupole phonons [41,58]. Both isotopic and isotonic dependencies of these values are not as strong as in the cases of the 0_1^+ and 2_1^+ states.

In Figs. 7(e) and 7(f) we notice that for the 1_1^- and 3_1^- states $1.5 \leqslant \langle \hat{n}_f \rangle \leqslant 2.0$ when $N < 140$. For larger values of N, $\langle \hat{n}_f \rangle$ gradually decreases to reach the value of 1 at $N \approx 150$. Therefore, we conclude that more than one f boson is needed for the employed EDF-to-IBM mapping procedure to reasonably describe excitation spectra of low-lying negative-parity yrast states in actinide nuclei with $N \leqslant 140$, while for heavier actinides, inclusion of only one f boson seems to suffice.

F. Possible alternating-parity band structure

To distinguish if the members of rotational bands are octupole-deformed or octupole vibrational states, it is convenient to consider the quantity

$$\delta E(J^-) = E(J^-) - \frac{E((J+1)^+) + E((J-1)^+)}{2}, \qquad (8)$$

where $E(J^-)$ and $E((J \pm 1)^+)$ represent excitation energies of the odd-spin negative-parity and even-spin positive-parity yrast states, respectively. If the positive- and negative-parity bands share an octupole-deformed band head they form an alternating-parity doublet and the quantity $\delta E(J^-)$ should

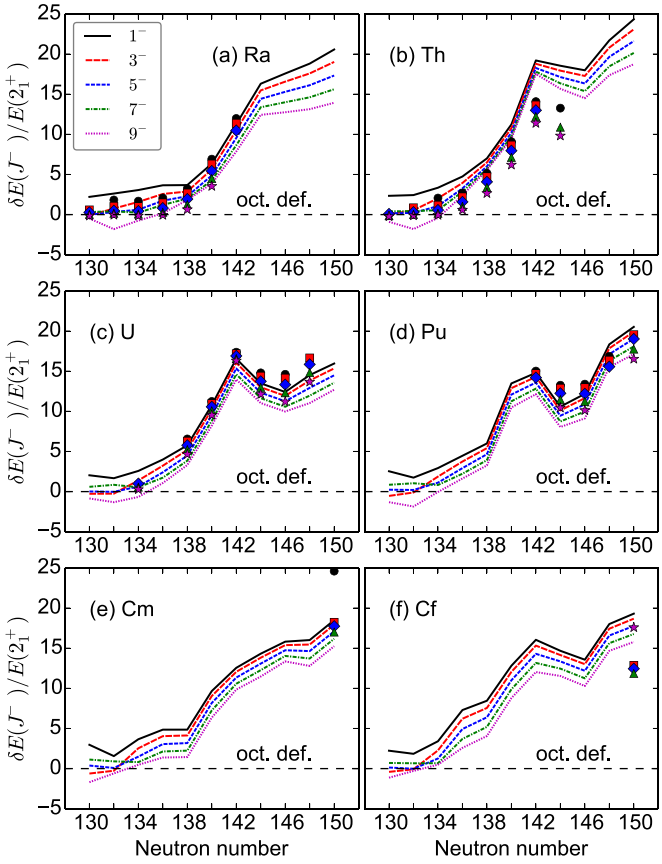

FIG. 8. The energy displacement $\delta E(J^-)$ [defined in Eq. (8)], normalized with respect to the excitation energy of the 2_1^+ state, is shown as a function of the neutron number. The theoretical values are connected by lines. The corresponding experimental [63] values for the $J^- = 1^-$, 3^-, 5^-, 7^-, and 9^- yrast states are represented by the solid circles, squares, diamonds, triangles, and stars, respectively. Results for the Ra and Th nuclei are from Ref. [45]. The limit of stable octupole deformation $\delta E(J^-) = 0$ is indicated in each panel by a broken horizontal line.

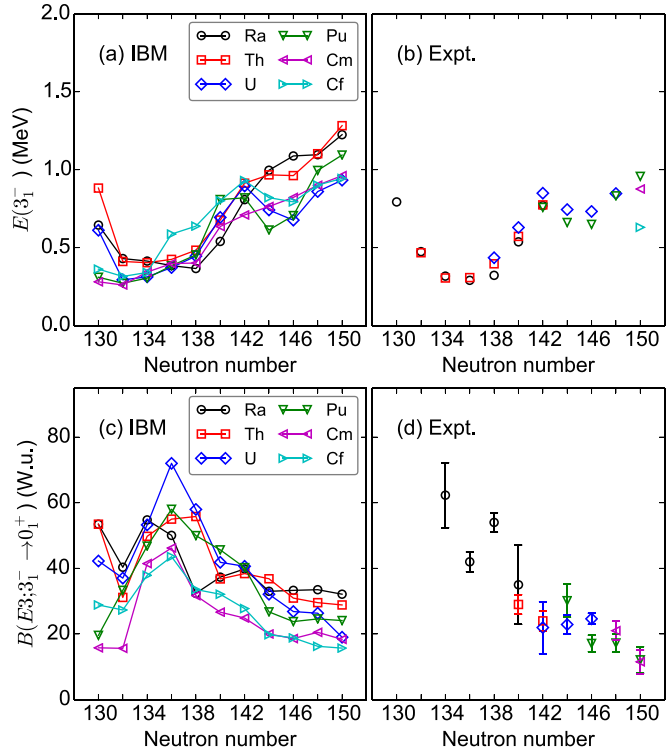

FIG. 9. Evolution of the (a) theoretical and (b) experimental excitation energy of the 3_1^- state, and the (c) theoretical and (d) experimental $B(E3;3_1^- \to 0_1^+)$ transition strength in Weisskopf units for the Ra, Th, U, Pu, Cm, and Cf isotopes as functions of the neutron number. Theoretical values for the Ra and Th nuclei are taken from Ref. [45]. The experimental data are from Refs. [63,64].

be equal to zero. The deviation from the limit $\delta E(J^-) = 0$ means that the positive- and negative-parity bands form separate bands, and therefore an octupole vibrational structure emerges. In Fig. 8, the calculated $\delta E(J^-)/E(2_1^+)$ values for the $J = 1_1^-$ to 9_1^- states are plotted as functions of N. Let us take as examples the results for the Ra and Th isotopic chains in Figs. 8(a) and 8(b). The ratios $\delta E(J^-)/E(2_1^+)$ for each spin are close to zero for a number of Ra and Th isotopes with neutron numbers below $N \approx 138$, i.e., $^{218-226}$Ra and $^{220-228}$Th. For heavier isotopes with $N \geqslant 140$, $\delta E(J^-)/E(2_1^+)$ values turn to increase with N. Thus the octupole vibrational states characterized by the octupole-soft potential appear. Essentially the same trend is observed for the U, Pu, Cm, and Cf isotopes.

G. Transition rates

Transition probabilities are computed with the electric dipole, quadrupole, and octupole transition operators $\hat{T}^{E\lambda} = e_\lambda \hat{Q}_\lambda$ ($\lambda = 1, 2, 3$). As in Ref. [45], the effective charge e_λ for $\lambda = 2$ and 3 depends on the boson number n, and is determined so that the IBM's intrinsic quadrupole (octupole) moments calculated at $\beta_\lambda = \beta_{\lambda,\min}$ coincide with the SCMF ones. Formulas used to determine the values of e_λ can be found in Ref. [45]. In the present calculations, a slight modification to the formulas given in Ref. [45] was considered: for the Cm and Cf isotopes, an overall factor of the e_2 charge was rescaled so that the experimental $B(E2;2_1^+ \to 0_1^+)$ values for ^{244,246}Cm are reasonably reproduced. The employed $e_{\lambda=2,3}$ values are also shown in Figs. 4(k) and 4(l). The $E1$ transition operator is defined in Ref. [45], and the same value of the $E1$ charge $e_1 = 0.0277 e\text{b}^{1/2}$ is used for all the considered isotopic chains. The $B(E3;3_1^- \to 0_1^+)$ transition rates as well as the excitation energies of the 3_1^- state are depicted as functions of N in Fig. 9. The predicted $B(E3)$ values show marked peaks at around $N = 136$ with a maximum value of 72 W.u. (Weisskopf units) for ^{228}U. This trend is correlated with the behaviors of the calculated and experimental $E(3_1^-)$ values plotted in Figs. 9(a) and 9(b): the $B(E3;3_1^- \to 0_1^+)$ values are inversely proportional to the $E(3_1^-)$ ones.

In addition, we compare in Fig. 10 the calculated and experimental $B(E2;2_1^+ \to 0_1^+)$ and $B(E1;1_1^- \to 0_1^+)$ values. The predicted $B(E2)$ rates keep increasing with N as the quadrupole collectivity develops, and are in a good agreement with the data. However, the present model is unable to describe, even qualitatively, the empirical $B(E1)$ rates

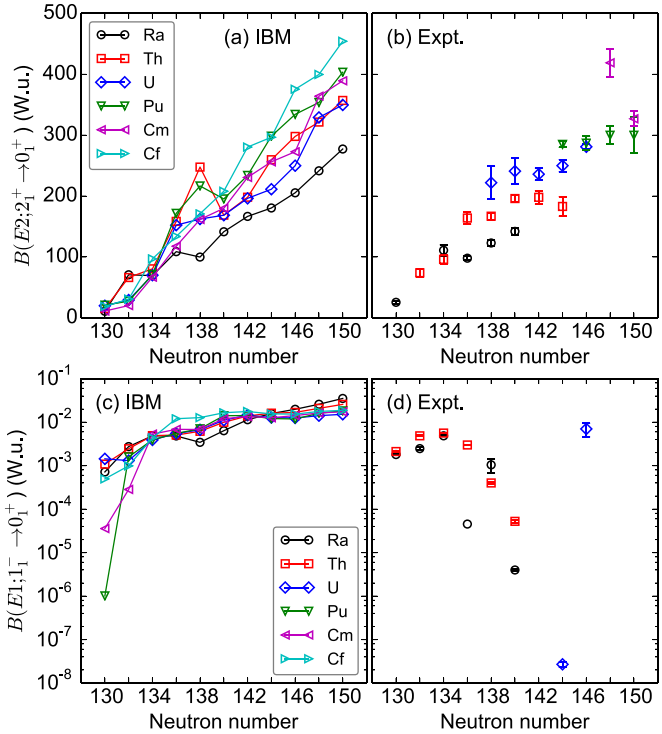

FIG. 10. Evolution of the (a) theoretical and (b) experimental $B(E2; 2_1^+ \to 0_1^+)$ and (c) theoretical and (d) experimental $B(E1; 1_1^- \to 0_1^+)$ transition strength in Weisskopf units for the Ra, Th, U, Pu, Cm, and Cf isotopes as functions of the neutron number. Theoretical values for the Ra and Th nuclei are taken from Ref. [45]. The experimental data are from Refs. [63].

[Figs. 10(c) and 10(d)]. This is mainly because of the fact that the $E1$ properties are less collective in nature, while the IBM framework is built on correlated pairs and deals with purely collective states. Another reason is that, within the *sdf* boson space, the $E1$ transition operator only contains a term that is proportional to $(d^\dagger \tilde{f} + f^\dagger \tilde{d})^{(1)}$, and this simplified form may not satisfactorily describe the details of the observed $B(E1)$ systematic. Inclusion of higher-order terms in the $E1$ operator or taking into account explicitly the dipole p boson with $J = 1^-$ could improve description of the $E1$ rates, but these extensions are clearly out of the scope of the present paper.

H. Effective quadrupole and octupole deformations

We further consider quadrupole and octupole shape invariants [65,66] calculated in the IBM ground state $|0_1^+\rangle$:

$$q_2^{(\lambda)} = \sum_i (-1)^J \langle 0_1^+ \| \hat{T}^{E\lambda} \| J_i^\pi \rangle \langle J_i^\pi \| \hat{T}^{E\lambda} \| 0_1^+ \rangle , \tag{9}$$

$$q_4^{(\lambda)} = \sum_{i,j,k} \langle 0_1^+ \| \hat{T}^{E\lambda} \| J_i^\pi \rangle \langle J_i^\pi \| \hat{T}^{E\lambda} \| 0_j^+ \rangle \times \langle 0_j^+ \| \hat{T}^{E\lambda} \| J_k^\pi \rangle \langle J_k^\pi \| \hat{T}^{E\lambda} \| 0_1^+ \rangle , \tag{10}$$

where $\langle 0^+ \| \hat{T}^{E\lambda} \| J^\pi \rangle$'s are reduced matrix elements of the $E\lambda$ transition operators, and $J^\pi = 2^+$ and 3^- for $\lambda = 2$ and 3, respectively. The sums in Eqs. (9) and (10) include up to ten lowest 0^+, 2^+, and 3^- states. We can define the effective quadrupole and octupole deformation parameters

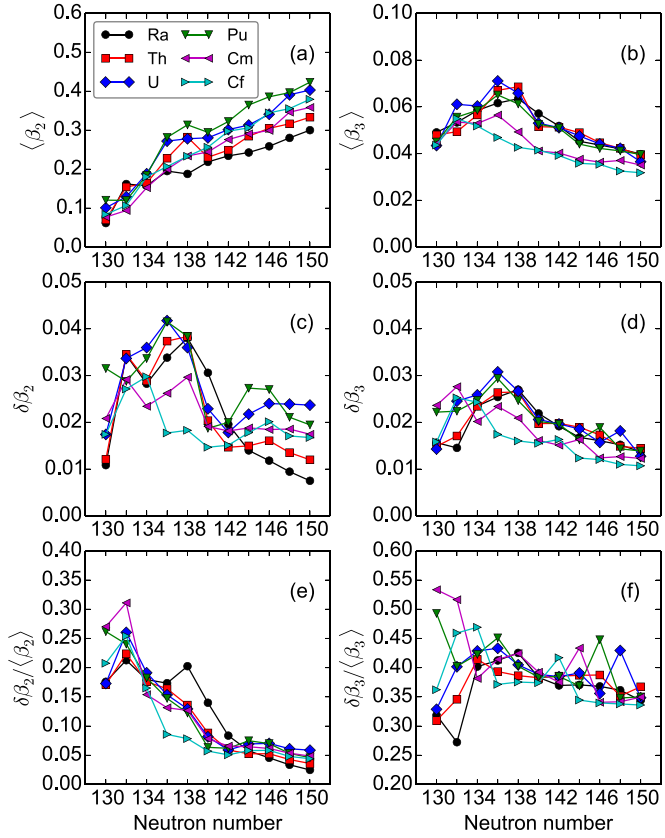

FIG. 11. Effective (a) quadrupole $\langle \beta_2 \rangle$ and (b) octupole $\langle \beta_3 \rangle$ deformation parameters, (c), (d) variance $\delta\beta_\lambda$, and (e), (f) the fluctuations $\delta\beta_\lambda / \langle \beta_\lambda \rangle$ for $^{218-238}$Ra, $^{220-240}$Th, $^{222-242}$U, $^{224-244}$Pu, $^{226-246}$Cm, and $^{228-248}$Cf, as functions of the neutron number. Values for the Ra and Th nuclei are calculated based on the results from Ref. [45]. See the main text for details.

$$\langle \beta_\lambda \rangle = \sqrt{\langle \beta_\lambda^2 \rangle} \tag{11}$$

and the variance

$$\delta\beta_\lambda = \sqrt{\langle \beta_\lambda^4 \rangle - \langle \beta_\lambda^2 \rangle^2} \Big/ 2 \langle \beta_\lambda \rangle , \tag{12}$$

where $\langle \beta_\lambda^{2m} \rangle = (4\pi/(3eZR_0^\lambda))^{2m} q_{2m}^{(\lambda)}$ $(m = 1, 2)$.

In Fig. 11 we display the above-mentioned quantities as functions of N: in Figs. 11(a) and 11(b) we show $\langle \beta_\lambda \rangle$ for $\lambda = 2$ and 3, respectively. In Figs. 11(c) and 11(d) the $\delta\beta_\lambda$ are displayed. Finally, the fluctuations $\delta\beta_\lambda / \langle \beta_\lambda \rangle$ are presented in Figs. 11(e) and 11(f). The effective quadrupole deformation $\langle \beta_2 \rangle$ increases monotonously with N as the quadrupole collectivity develops. The behavior of the effective octupole deformation parameter $\langle \beta_3 \rangle$ for each isotopic chain is characterized by a parabolic trend with a marked peak at $N \approx 136$. The behavior of these quantities with neutron number is in agreement with the one of the intrinsic deformation parameters shown in Fig. 3. The variance for both the quadrupole and octupole deformations is large from $N \approx 132$ to $N \approx 140$. In such transitional regions, potentials are soft in both β_2 and β_3

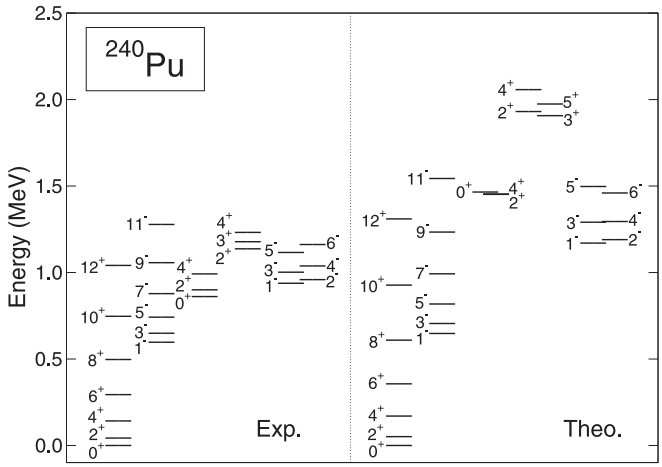

FIG. 12. Comparison of theoretical and experimental low-energy level schemes of ^{240}Pu.

(cf. Figs. 1 and 2), and large shape fluctuations are present. This is confirmed by rapid changes of the quantities $\delta\beta_2/\langle\beta_2\rangle$ and $\delta\beta_3/\langle\beta_3\rangle$ between $N \approx 132$ and $N \approx 138$ [cf. Figs. 11(e) and 11(f)].

I. Detailed level scheme of ^{240}Pu

Finally, we examine the ability of the present approach to describe detailed spectroscopy in individual nuclei. As an illustrative example, in Fig. 12 we compare theoretical and experimental low-energy level schemes of ^{240}Pu. A good agreement between theory and experiment is observed in the lowest-lying members of the positive- and negative-parity rotational bands, as well as in the band built on the 1^-_2 state. The model, however, considerably overestimates the bandhead energies of the excited $K^\pi = 0^+$ band built on the 0^+_2 state and the γ-vibrational ($K^\pi = 2^+$) band on top of 2^+_3. The discrepancies in the $K^\pi = 0^+$ and 2^+ bands are most likely related to the fact that the underlying SCMF-PESs have too steep potentials to be reproduced by the IBM ones. The description of the γ-band levels could be partly improved by explicitly taking into account the triaxial degree of freedom in the present calculation. It has been shown [67] that a specific form of three-body boson term plays an important role to lower the γ band. As we have seen in Figs. 7(c) and 7(d), the IBM wave functions of the 0^+_2 state and the band built on it for most of the considered actinide nuclei are mainly based on two-octupole-boson configurations. However, the fact that the 0^+_2 energy is overestimated may indicate a need for including additional building blocks in the IBM framework to improve the agreement with experimental results. For instance, inclusion of the dynamical pairing degree of freedom in the IBM model space has been shown [68] to have a significant impact on the description of the excited 0^+ states.

We note that, except for the heavier isotopes Cm and Cf, plenty of spectroscopic data are available for the neighboring U and Pu nuclei as well. We have then carried out similar analyses, and confirmed that the level of agreement between the predicted and experimental energy levels with both parities for these nuclei is similar to ^{240}Pu, while the same problem as seen in ^{240}Pu is commonly observed, that is, both the excited 0^+ and 2^+ bands are considerably overestimated within the mapped IBM framework.

IV. SUMMARY

Octupole shapes and collective excitations in the actinide nuclei Ra, Th, U, Pu, Cm, and Cf with neutron number $130 \leqslant N \leqslant 150$ were investigated by using the EDF-based IBM framework. Axially symmetric quadrupole β_2 and octupole β_3 SCMF-PESs, obtained from constrained HFB calculations based on the Gogny-D1M EDF, were used to determine the *sdf*-IBM Hamiltonian. Diagonalization of the mapped Hamiltonian produces excitation spectra and transition strengths. The Gogny-D1M SCMF-PESs have suggested transitions from nearly spherical ($N \approx 130$) to stable octupole-deformed ($N \approx 134$) and to octupole-soft ($N \approx 138$) shapes along the considered U, Pu, Cm, and Cf isotopic chains. Consistently with the empirical tendency, the calculated negative-parity yrast states show a parabolic trend centered at $N \approx 136$, and the $B(E3; 3^-_1 \to 0^+_1)$ transition rates are predicted to take maximal values around $N \approx 136$, where the SCMF-PESs exhibit the most pronounced octupole minima. The rotational bands of a number of nuclei exhibit the alternating-parity pattern associated with a rigid octupole shape (cf. Fig. 8). The effective β_2 and β_3 deformations and their variance suggest large shape fluctuations near $N = 134$. All the spectroscopic properties obtained from the mapped *sdf*-IBM Hamiltonian exhibit tendencies that correlate with the variation of the Gogny-D1M SCMF-PESs, and consistently suggest the onset of stable octupole deformation around $N = 136$ and that the transitions between octupole-deformed and octupole-soft shapes occur systematically in the actinide region. The spectroscopic results discussed in this paper also agree well, at least qualitatively, with the recent EDF-based spectroscopic calculations [34,38] that covered the same region of nuclei as the one studied here.

Even though our model allows for a detailed and economic description of octupole-related spectroscopic properties, the current implementation of the model is not able to describe quantitatively the spectra of nonyrast states. For instance, the model has overestimated considerably the excitation energies of the 0^+_2 states and the $\gamma(K = 2^+)$ band (cf. Fig. 12). This implies the necessity of including those building blocks that are beyond the considered IBM framework, e.g., dynamical pairing and triaxial degrees of freedom (i.e., higher-order terms in the IBM Hamiltonian). Since these new building blocks have negligible contributions to the yrast states with both parities, they would not alter the conclusion of the present work; that is, the stable octupole shape occurs around $N \approx 134$ and octupole softness emerges around $N \approx 138$ in actinide nuclei. Such extensions of the model will be required for a complete spectroscopic study that involves an accurate description of excitation energies and transition rates of nonyrast states. Another interesting topic is to extend the analysis to odd-mass actinides. Work along these lines is in progress, and will be reported in forthcoming articles.

ACKNOWLEDGMENTS

This work has been supported by the Tenure Track Pilot Programme of the Croatian Science Foundation and the École Polytechnique Fédérale de Lausanne, and the Project TTP-2018-07-3554 Exotic Nuclear Structure and Dynamics, with funds of the Croatian-Swiss Research Programme. The work of L.M.R. was supported by Spanish Ministry of Economy and Competitiveness (MINECO) Grant No. PGC2018-094583-B-I00. This work has been partially supported by the Ministerio de Ciencia e Innovación (Spain) under Projects No. PID2019-104002GB-C21, by the Consejería de Economía, Conocimiento, Empresas y Universidad de la Junta de Andalucía (Spain) under Group FQM-370, by the European Regional Development Fund (ERDF), SOMM17/6105/UGR, and by the European Commission, H2020-INFRAIA-2014-2015 (ENSAR2). Resources supporting this work were provided by the CEAFMC and the Universidad de Huelva High Performance Computer (HPC@UHU) funded by ERDF/MINECO project UNHU-15CE-2848.

[1] P. A. Butler and W. Nazarewicz, Rev. Mod. Phys. **68**, 349 (1996).

[2] P. A. Butler, J. Phys. G: Nucl. Part. Phys. **43**, 073002 (2016).

[3] L. P. Gaffney, P. A. Butler, M. Scheck, A. B. Hayes, F. Wenander, M. Albers, B. Bastin, C. Bauer, A. Blazhev, S. Bönig, N. Bree, J. Cederkäll, T. Chupp, D. Cline, T. E. Cocolios, T. Davinson, H. D. Witte, J. Diriken, T. Grahn, A. Herzan, M. Huyse, D. G. Jenkins, D. T. Joss, N. Kesteloot, J. Konki, M. Kowalczyk, T. Kröll, E. Kwan, R. Lutter, K. Moschner, P. Napiorkowski, J. Pakarinen, M. Pfeiffer, D. Radeck, P. Reiter, K. Reynders, S. V. Rigby, L. M. Robledo, M. Rudigier, S. Sambi, M. Seidlitz, B. Siebeck, T. Stora, P. Thoele, P. V. Duppen, M. J. Vermeulen, M. von Schmid, D. Voulot, N. Warr, K. Wimmer, K. Wrzosek-Lipska, C. Y. Wu, and M. Zielinska, Nature (London) **497**, 199 (2013).

[4] P. A. Butler, L. P. Gaffney, P. Spagnoletti, K. Abrahams, M. Bowry, J. Cederkäll, G. de Angelis, H. De Witte, P. E. Garrett, A. Goldkuhle, C. Henrich, A. Illana, K. Johnston, D. T. Joss, J. M. Keatings, N. A. Kelly, M. Komorowska, J. Konki, T. Kröll, M. Lozano, B. S. Nara Singh, D. O'Donnell, J. Ojala, R. D. Page, L. G. Pedersen, C. Raison, P. Reiter, J. A. Rodriguez, D. Rosiak, S. Rothe, M. Scheck, M. Seidlitz, T. M. Shneidman, B. Siebeck, J. Sinclair, J. F. Smith, M. Stryjczyk, P. Van Duppen, S. Vinals, V. Virtanen, N. Warr, K. Wrzosek-Lipska, and M. Zielińska, Phys. Rev. Lett. **124**, 042503 (2020).

[5] M. M. R. Chishti, D. O'Donnell, G. Battaglia, M. Bowry, D. A. Jaroszynski, B. S. N. Singh, M. Scheck, P. Spagnoletti, and J. F. Smith, Nat. Phys. **16**, 853 (2020).

[6] B. Bucher, S. Zhu, C. Y. Wu, R. V. F. Janssens, D. Cline, A. B. Hayes, M. Albers, A. D. Ayangeakaa, P. A. Butler, C. M. Campbell, M. P. Carpenter, C. J. Chiara, J. A. Clark, H. L. Crawford, M. Cromaz, H. M. David, C. Dickerson, E. T. Gregor, J. Harker, C. R. Hoffman, B. P. Kay, F. G. Kondev, A. Korichi, T. Lauritsen, A. O. Macchiavelli, R. C. Pardo, A. Richard, M. A. Riley, G. Savard, M. Scheck, D. Seweryniak, M. K. Smith, R. Vondrasek, and A. Wiens, Phys. Rev. Lett. **116**, 112503 (2016).

[7] B. Bucher, S. Zhu, C. Y. Wu, R. V. F. Janssens, R. N. Bernard, L. M. Robledo, T. R. Rodríguez, D. Cline, A. B. Hayes, A. D. Ayangeakaa, M. Q. Buckner, C. M. Campbell, M. P. Carpenter, J. A. Clark, H. L. Crawford, H. M. David, C. Dickerson, J. Harker, C. R. Hoffman, B. P. Kay, F. G. Kondev, T. Lauritsen, A. O. Macchiavelli, R. C. Pardo, G. Savard, D. Seweryniak, and R. Vondrasek, Phys. Rev. Lett. **118**, 152504 (2017).

[8] W. Nazarewicz, P. Olanders, I. Ragnarsson, J. Dudek, G. A. Leander, P. Möller, and E. Ruchowsa, Nucl. Phys. A **429**, 269 (1984).

[9] G. Leander, W. Nazarewicz, P. Olanders, I. Ragnarsson, and J. Dudek, Phys. Lett. B **152**, 284 (1985).

[10] P. Möller, R. Bengtsson, B. Carlsson, P. Olivius, T. Ichikawa, H. Sagawa, and A. Iwamoto, At. Dat. Nucl. Dat. Tab. **94**, 758 (2008).

[11] S. Marcos, H. Flocard, and P. Heenen, Nucl. Phys. A **410**, 125 (1983).

[12] P. Bonche, P. Heenen, H. Flocard, and D. Vautherin, Phys. Lett. B **175**, 387 (1986).

[13] P. Bonche, S. J. Krieger, M. S. Weiss, J. Dobaczewski, H. Flocard, and P.-H. Heenen, Phys. Rev. Lett. **66**, 876 (1991).

[14] P.-H. Heenen, J. Skalski, P. Bonche, and H. Flocard, Phys. Rev. C **50**, 802 (1994).

[15] L. M. Robledo, J. L. Egido, J. Berger, and M. Girod, Phys. Lett. B **187**, 223 (1987).

[16] L. M. Robledo, J. L. Egido, B. Nerlo-Pomorska, and K. Pomorski, Phys. Lett. B **201**, 409 (1988).

[17] J. L. Egido and L. M. Robledo, Nucl. Phys. A **518**, 475 (1990).

[18] J. L. Egido and L. M. Robledo, Nucl. Phys. A **524**, 65 (1991).

[19] J. L. Egido and L. M. Robledo, Nucl. Phys. A **545**, 589 (1992).

[20] E. Garrote, J. L. Egido, and L. M. Robledo, Phys. Rev. Lett. **80**, 4398 (1998).

[21] E. Garrote, J. L. Egido, and L. M. Robledo, Nucl. Phys. A **654**, 723c (1999).

[22] W. Long, J. Meng, N. Van Giai, and S.-G. Zhou, Phys. Rev. C **69**, 034319 (2004).

[23] L. M. Robledo, M. Baldo, P. Schuck, and X. Viñas, Phys. Rev. C **81**, 034315 (2010).

[24] L. M. Robledo and G. F. Bertsch, Phys. Rev. C **84**, 054302 (2011).

[25] J. Erler, K. Langanke, H. P. Loens, G. Martínez-Pinedo, and P.-G. Reinhard, Phys. Rev. C **85**, 025802 (2012).

[26] L. M. Robledo and R. R. Rodríguez-Guzmán, J. Phys. G: Nucl. Part. Phys. **39**, 105103 (2012).

[27] R. Rodríguez-Guzmán, L. M. Robledo, and P. Sarriguren, Phys. Rev. C **86**, 034336 (2012).

[28] L. M. Robledo and P. A. Butler, Phys. Rev. C **88**, 051302(R) (2013).

[29] L. M. Robledo, J. Phys. G: Nucl. Part. Phys. **42**, 055109 (2015).

[30] R. N. Bernard, L. M. Robledo, and T. R. Rodríguez, Phys. Rev. C **93**, 061302(R) (2016).

[31] S. E. Agbemava, A. V. Afanasjev, and P. Ring, Phys. Rev. C **93**, 044304 (2016).

[32] S. E. Agbemava and A. V. Afanasjev, Phys. Rev. C **96**, 024301 (2017).

[33] Z. Xu and Z.-P. Li, Chin. Phys. C **41**, 124107 (2017).

[34] S. Y. Xia, H. Tao, Y. Lu, Z. P. Li, T. Nikšić, and D. Vretenar, Phys. Rev. C **96**, 054303 (2017).
[35] S. Ebata and T. Nakatsukasa, Phys. Scr. **92**, 064005 (2017).
[36] R. Rodríguez-Guzmán, Y. M. Humadi, and L. M. Robledo, Eur. Phys. J. A **56**, 43 (2020).
[37] Y. Cao, S. E. Agbemava, A. V. Afanasjev, W. Nazarewicz, and E. Olsen, Phys. Rev. C **102**, 024311 (2020).
[38] R. Rodríguez-Guzmán, Y. M. Humadi, and L. M. Robledo, J. Phys. G: Nucl. Part. Phys. **48**, 015103 (2020).
[39] J. Engel and F. Iachello, Nucl. Phys. A **472**, 61 (1987).
[40] N. V. Zamfir and D. Kusnezov, Phys. Rev. C **63**, 054306 (2001).
[41] N. V. Zamfir and D. Kusnezov, Phys. Rev. C **67**, 014305 (2003).
[42] K. Nomura, D. Vretenar, and B.-N. Lu, Phys. Rev. C **88**, 021303(R) (2013).
[43] K. Nomura, D. Vretenar, T. Nikšić, and B.-N. Lu, Phys. Rev. C **89**, 024312 (2014).
[44] K. Nomura, R. Rodríguez-Guzmán, and L. M. Robledo, Phys. Rev. C **92**, 014312 (2015).
[45] K. Nomura, R. Rodríguez-Guzmán, Y. M. Humadi, L. M. Robledo, and J. E. García-Ramos, Phys. Rev. C **102**, 064326 (2020).
[46] D. Bonatsos, D. Lenis, N. Minkov, D. Petrellis, and P. Yotov, Phys. Rev. C **71**, 064309 (2005).
[47] D. Lenis and D. Bonatsos, Phys. Lett. B **633**, 474 (2006).
[48] P. G. Bizzeti and A. M. Bizzeti-Sona, Phys. Rev. C **88**, 011305(R) (2013).
[49] T. M. Shneidman, G. G. Adamian, N. V. Antonenko, R. V. Jolos, and W. Scheid, Phys. Lett. B **526**, 322 (2002).
[50] T. M. Shneidman, G. G. Adamian, N. V. Antonenko, R. V. Jolos, and W. Scheid, Phys. Rev. C **67**, 014313 (2003).
[51] K. Nomura, N. Shimizu, and T. Otsuka, Phys. Rev. Lett. **101**, 142501 (2008).
[52] F. Iachello and A. Arima, *The Interacting Boson Model* (Cambridge University Press, Cambridge, UK, 1987).
[53] T. Nikšić, D. Vretenar, and P. Ring, Phys. Rev. C **78**, 034318 (2008).
[54] S. Goriely, S. Hilaire, M. Girod, and S. Péru, Phys. Rev. Lett. **102**, 242501 (2009).
[55] P. Ring and P. Schuck, *The Nuclear Many-Body Problem* (Springer-Verlag, Berlin, 1980).
[56] M. Bender, P.-H. Heenen, and P.-G. Reinhard, Rev. Mod. Phys. **75**, 121 (2003).
[57] L. M. Robledo, T. R. Rodríguez, and R. R. Rodríguez-Guzmán, J. Phys. G: Nucl. Part. Phys. **46**, 013001 (2019).
[58] M. Spieker, S. Pascu, D. Bucurescu, T. M. Shneidman, T. Faestermann, R. Hertenberger, H.-F. Wirth, N.-V. Zamfir, and A. Zilges, Phys. Rev. C **97**, 064319 (2018).
[59] J. N. Ginocchio and M. W. Kirson, Nucl. Phys. A **350**, 31 (1980).
[60] S. Heinze, computer program ARBMODEL, University of Cologne, 2008.
[61] J. F. Berger, M. Girod, and D. Gogny, Nucl. Phys. A **428**, 23 (1984).
[62] F. Chappert, M. Girod, and S. Hilaire, Phys. Lett. B **668**, 420 (2008).
[63] Brookhaven National Nuclear Data Center, http://www.nndc.bnl.gov.
[64] T. Kibédi and R. Spear, At. Data Nucl. Data Tables **80**, 35 (2002).
[65] D. Cline, Annu. Rev. Nucl. Part. Sci. **36**, 683 (1986).
[66] V. Werner, N. Pietralla, P. von Brentano, R. F. Casten, and R. V. Jolos, Phys. Rev. C **61**, 021301(R) (2000).
[67] K. Nomura, N. Shimizu, D. Vretenar, T. Nikšić, and T. Otsuka, Phys. Rev. Lett. **108**, 132501 (2012).
[68] K. Nomura, D. Vretenar, Z. P. Li, and J. Xiang, Phys. Rev. C **102**, 054313 (2020).